Two-dimensional simulations of temperature and current-density distribution in electromigrated structures

Two-dimensional simulations of temperature and current-density distribution in electromigrated structures

Birgit Kießig[1,2]**, Roland Schäfer**[1,3] **and Hilbert von Löhneysen**[1,2]

[1] Karlsruhe Institute of Technology, Institut für Festkörperphysik, D-76021 Karlsruhe, Germany
[2] Karlsruhe Institut of Technology, Physikalisches Institut, D-76131 Karlsruhe, Germany
E-mail: Roland.Schaefer@kit.edu

Abstract

We report on the application of a feedback-controlled electromigration technique for the formation of nanometre-sized gaps in mesoscopic gold wires and rings. The effect of current density and temperature, linked via Joule heating, on the resulting gap size is investigated. Our experiments include *in situ* measurements of the evolution of the electrical resistance and of the structure of the device during electromigration. Experimentally, a good thermal coupling to the substrate turned out to be crucial to reach electrode spacings below 10 nm and to avoid overall melting of the nanostructures. This finding is supported by numerical calculations of the current-density and temperature profiles for structure layouts subjected to electromigration. The numerical method can be used for optimizing the layout so as to predetermine the location where electromigration leads to the formation of a gap.

S Online supplementary data available from stacks.iop.org/NJP/16/013017/mmedia

[3] Author to whom any correspondence should be addressed.

1. Introduction

The diffusive flow of atoms in metals is driven by several forces one of which is proportional and parallel to the electric field. This force is partially of electrostatic nature due to the positive charge of the atomic cores but is in most cases dominated by the so called 'electron wind': the diffusive motion of the conduction electrons has a net direction (namely that of the macroscopic current density) in response to the electric field; the scattering at lattice defects leads to a momentum transfer between the electrons and atoms driving the latter in anode direction. It is this effect which is referred to as electromigration (EM) [1, 2] in the literature. The migration is almost entirely due to a vacancy exchange mechanism [3] and the material flux can be described in terms of a vacancy flux $\boldsymbol{J}_v$ [4].

EM is of high technological importance for the semiconductor industry since interconnects in integrated circuits are made of metals (mainly aluminium or more recently copper) with ever increasing current densities during normal operation. EM can lead to accumulation and depletion of material at position of flux divergence, which is strongest at grain boundaries and at the joints of three grains [5]. Depletion results ultimately in the formation of voids and line failure. Modelling EM has therefore a long tradition and has reached a high level of maturity [4]. The focus has naturally been on how to avoid or delay deterioration of interconnects, i.e. electrical lines of mostly constant cross section meandering in two or three dimensions. In general, the interconnects are embedded in dielectrics so that all surfaces form interfaces with solids. This can increase the resistance to EM considerably due to a counterflow related to the mechanical stress [6] which is stabilized by the confining envelope.

However, for more than a decade [7], EM has been employed to deliberately form gaps of the order of a few nanometres only in microstructures. These gaps can be used to incorporate molecules in a source–drain channel. The planar geometry facilitates the integration of gating electrodes that are essential for a systematic characterization of electronic transport through molecules. This type of experiments start in general with planar metallic structures (gold being the most widely used material) on an insulating structure and the opposite surface is in contact to vacuum or a gaseous atmosphere. The goal of EM is to form a gap at a more or less well defined position and width. To this end the planar layout contains a constricted region to yield high current densities and strong Joule heating at the same time. Since $\boldsymbol{J}_v$ is proportional to the vacancy diffusion coefficient D_v which obeys an Arrhenius type of temperature dependence, $D_v \propto \exp(-E_a/k_B T)$, EM is strongly temperature dependent. E_a is an activation energy, k_B the Boltzmann constant and T the absolute temperature. Thus, $\boldsymbol{J}_v$ is large in regions of elevated temperature and high current densities. It is normally assumed that stress cannot build up over the regions of highest diffusivity in gold [8, 9] since hillocks at the anode side of the surface easily build up releasing the stress. This in turn leads to depletion of material at the cathode side leading to void nucleation preferably at grain boundaries located in regions of high current densities and temperature gradients, followed by void grows, and finally a breaking up of a gap.

Initially, electromigration-induced break junctions (EIBJ) were fabricated in an cryogenic environment and irregularly shaped slits with a narrowest separation a were reported. From low-temperature current–voltage measurements, $a \sim 1$ nm was estimated [7, 10]. However, metallic clusters often remained in the generated gap [11–13]. By working at room temperature, the cleanliness of the gaps could be improved. However, special care has to be taken so as to limit the dissipated power during void growth. While the smallest cross section of the structure is

shrinking the total current has to be reduced accordingly. Otherwise the ever increasing current density leads at some point to fatal heating and the break junction is produced by melting rather than EM. The gap is in general far to large in this case. Power control has been achieved either by active feedback [5, 14–17] or by eliminating the influence of serial resistance by monitoring the voltage drop over the narrow constriction [18, 19].

Hence, to obtain a high yield of nanogaps, the experimental parameters have to be optimized with respect to two competing objectives. On the one hand, the temperature T and the current density j have to be raised sufficiently for material transport to occur on a reasonable time scale. On the other hand, Joule heating has to be limited to avoid melting of the metal structure, which would lead to droplet formation due to surface tension and to an unwanted increase in electrode spacing. Several authors attempted to deduce the temperature at which EIBJ form. One method uses the resistance change at high bias as a measure of temperature by using a previously calibrated T versus R relation [18, 20–22]. This method is problematic, though, since firstly the temperature of the self-heated structure is not constant but varies in the same way as the current density; thus the resistance change measures at best an average temperature of the structure while—due to the exponential factor in the Arrhenius law—the maximal temperature is what matters most. Secondly, the temperature calibration implicitly depends on the disorder scattering which in general changes during EM. Thus the calibration can change in the course of the experiment. In one case [18], the total loss of calibration is obvious. Taychatanapat *et al* [19] cover their gold structures with nanoclusters. By heating test layers to different temperatures they determine the temperature T^* at which the clusters are dissolved by the gold layer. When the current I is increased during the EIBJ formation the nanoclusters are dissolved at a specific I value; the authors can thus pinpoint a current density at which the structure is heated to T^* which is in fact a lower bound for the temperature during EM. Other authors use numerical simulations to estimate a temperature profile in EIBJ layouts. The used electro-thermal models range from simple one-dimensional approximations [20] to more sophisticated finite-element models [5, 23].

In this paper we report on EIBJ experiments and electro-thermal simulations. Our experimental technique is similar to the one described in [17] aimed at the control of the power dissipated while the gap is being formed. Our final goal is to extend the technique used so far for gaps in single wires, to more complicated structures, e.g. to form gaps in the two arms of a ring connected by leads at opposite sides. In our experiments, we find a clear dependence of the resulting gap size on the thermal coupling of the electromigrated structure to the cold substrate. This coupling changes as a function of the thickness of a non-conductive layer insulating the metallic structure from the semiconducting substrate (p-doped silicon in our case). We present electro-thermal simulations which leads to a plausible explanation of this finding. It maps the current density and the excess temperature in the voltage-biased structure taking into account the heat flow through the insulator to the substrate. The calculations can be used to optimize the sample geometry so as to predetermine the location where EM leads to the formation of voids and the structure is finally going to break.

2. Experimental observations

All samples used for this work were prepared by standard e-beam lithography on commercially available, slightly p-doped (boron, resistivity: 1–20 Ω cm) silicon substrates. Their surface was either covered by 400 nm thermally grown SiO_2 or merely by native silicon oxide. Here, we
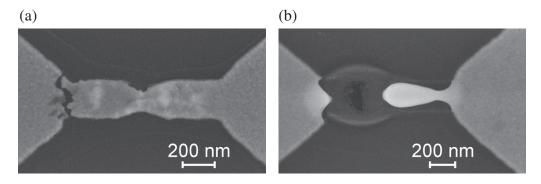
(a)　　　　　　　　　　　　　　　　　(b)

Figure 1. SEM images of gold wires after EM in high vacuum (10^{-5} mbar). The substrate consists of p-doped silicon covered by (a) native SiO_2 and (b) 400 nm thermally grown SiO_2, respectively. The brighter spots in (a) represent hillocks formed during EM. The bright metal blob in (b) results from droplet formation of liquid gold after the wire constriction had been destroyed by overheating. Pictures shown here are stills taken from the videos available as supplementary material from stacks.iop.org/NJP/16/013017/mmedia.

focus on samples made from 30 nm thick gold deposited by electron-beam evaporation without any additional adhesion layer.

We report on experiments performed at room temperature and mostly at ambient pressure. Some experiments were carried out in the high vacuum (10^{-3} Pa) of a scanning electron microscope (SEM) for *in situ* monitoring of the EM process. The resulting gap size, however, did not depend on the background pressure. The active feedback-control loop was realized by ramping a voltage across the sample and measuring its resistance in a four-point configuration. Upon detection of a certain change of $\Delta R/R \sim$ 5–10%, the voltage was set back to a safe value immediately by the control software and the voltage ramp was reinitialized. At an advanced stage of the process a sudden change of resistance by several orders of magnitude indicates rupture of the metallic current path and the procedure is stopped.

In this paper we discuss the influence of Joule heating during EM. Its effect manifested itself mainly in two aspects of our experiments. On the one hand, SEM imaging after gap formation revealed that metallic structures on silicon wafers covered by a 400 nm thick thermally grown silicon oxide layer show signs of melting. Consequently, the resulting electrode separation is considerably above 10 nm. A typical example—confirmed in more than 15 experiments—is shown in figure 1(b). This particular micrograph was taken by a SEM during the course of an *in situ* process; the full sequence of micrographs together with the corresponding V/R characteristics have been used to produce a video clip (see supplementary material). Samples electromigrated on silicon covered by native oxide, however, display the intended formation of voids and hillocks leading to the opening of an irregular gap, whose expansion lies below the resolution of the SEM, i.e. $a \lesssim 10$ nm. An example is shown in figure 1(a). On the other hand, as can be seen in the same figure, the samples were usually disrupted near their cathode end and not at the constriction prestructured for this purpose at the centre of the wire. EIBJ have been fabricated successfully in many experiments on native oxide and the particular example of figure 1(a) has been chosen from an EM experiment performed *in situ* in the vacuum of the SEM; the corresponding video clip is supplied as supplementary material.

Breaking at the cathode side is a common observation in *straight* wires [1, 24–27] of constant cross section and consequently constant current density. If such wires are connected at both ends to wider leads with low current densities self heating is largely restricted to the wire itself; EM as a strongly temperature dependent phenomena is then effective within the wire only where it leads to material flow in anode direction. Consequently material flows away from the cathode side and this loss is not balanced by incoming fresh material since flow entering from the wider leads is blocked due to their lower temperature. The purpose of the constriction shown in the centre of figure 1(b) is to enhance the current density and create a hot spot at a predefined position. Electromigration was expected to lead to a break junction at this very location which, however, was not observed. Apparently, the conditions at the lead-nanowire-junction have to be taken into account more carefully.

In the next section we present a model to calculate the temperature profile for a given sample layout which takes into account the heat flow from the metal film to the leads as well as to the substrate. The latter part is of utmost importance as indicated by our experimental observations presented in figure 1. The amount of heat flowing to the substrate changes with the thickness of the insulating barrier between the structure and the silicon substrate and has a remarkable effect on success or failure of EIBJ formation. To our knowledge, this aspect has not been addressed in a systematic manner so far.

3. Calculation of the heat distribution

The temperature in a voltage-biased sample is enhanced due to Joule heating. We present a model to quantify this effect. It is applicable to metallic structures of constant thickness d, sheet resistance $R_\square$ and thermal conductivity k_m. Heat is carried along the metal film to the leads and through an insulating barrier of thickness b and thermal conductivity k_b, where the condition $k_\mathrm{b} \ll k_\mathrm{m}$ naturally holds. The structure is supported below the barrier by a thick substrate with thermal conductivity k_s. The substrate is assumed to be thermally well coupled at the back side to a heat reservoir at ambient temperature. It is heated from the top by the power flowing through the barrier which results from the dissipation in the metallic structure. The situation in the substrate is therefore intrinsically three dimensional (3D). However, we can safely assume that the temperature in the metallic structure itself does not vary significantly perpendicular to the film plain (owing to $k_\mathrm{b} \ll k_\mathrm{m}$). The temperature rise in the substrate depends strongly on the barrier thickness b and is significant for small b only. We postpone the discussion of thicker barriers to the end of this section and assume first that the temperature varies linearly across the insulating barrier, i.e. we consider a laminar heat flow across the insulator perpendicular to its interfaces with the metal film and the substrate. The numerics for the metallic film is reduced to a two-dimensional problem obeying the modified Poisson equation:

$$k_\mathrm{m} d \nabla^2 \delta T + \dot{q} = \frac{k_\mathrm{b}}{b}(\delta T - \delta T_\mathrm{s}). \tag{1}$$

Here $\delta T(\boldsymbol{r})$ is the temperature elevation relative to the base temperature of the unbiased sample, $\dot{q} = \mathbf{j}^2 R_\square$ the power density, $\boldsymbol{j}(\boldsymbol{r})$ the two-dimensional current density, and $\delta T_\mathrm{s}(\boldsymbol{r})$ the temperature elevation at the interface between of the substrate and the barrier. The left-hand side of (1) describes the heat balance in the metallic film, while the right-hand side is equal to the loss due to heat flow to the substrate. The latter depends implicitly on $\delta T_\mathrm{s}(\boldsymbol{r})$ which itself

obeys the 3D Laplace equation (describing the source-free heat flow in the thick substrate)

$$\nabla^2 \delta T_{\mathrm{s}} = 0 \tag{2}$$

subjected to mixed boundary conditions. At the interface with the insulating barrier we have

$$\nabla_{\boldsymbol{n}} \delta T_{\mathrm{s}} = \frac{k_{\mathrm{b}}}{bk_{\mathrm{s}}}(\delta T_{\mathrm{s}} - \delta T), \tag{3}$$

where $\nabla_{\boldsymbol{n}}$ is the gradient perpendicular to the interface. At all other boundaries we approximate $\delta T_{\mathrm{s}}(\boldsymbol{r})$ by zero. Equations (1) and (2) form a set of mutually dependent relations.

We find it convenient to solve this set of equations by a finite-difference method on a square lattice and discretize the relevant parts of the metallic structure with a predefined cell size sufficiently small to capture all fine details. For this purpose we use an appropriate rectangular cutout of the e-beam lithography design file, which covers the area of highest current densities. For the examples presented below, a cell size between 1 and 5 nm turned out to be reasonable, with several million cells within the cutout. The current and voltage leads (cf horizontal and vertical structures, respectively, emanating from the centre in figure 2) have constant cross section and extend beyond the cutout. In addition the length of the leads included in the explicit calculation exceeds their width. These measures guarantee that the equipotential lines beyond the cutout generated by an electromotive force between source and drain current leads run perpendicular to the latter.

Before solving (1) and (2) we have to calculate the current density $\boldsymbol{j}$ which enters the second term on the left-hand side of (1). $\boldsymbol{j}$ is directly related by $\boldsymbol{j} = \nabla V / R_{\square}$ to the potential V, which in turn obeys the Laplace equation $\nabla^2 V = 0$ with mixed boundary conditions. We solve the latter equation by successive overrelaxation [28]. For edges of the metallic structure internal to the explicitly treated area as well as for sections of voltage probes with its border we have von-Neumann conditions, $\nabla_{\boldsymbol{n}} V = 0$. At the section of the source and drain leads with the border we apply the actual bias V_{max} and V_{min}, respectively. After solving the Laplace equation subjected to these boundary conditions, the total current $I = \int \mathrm{d}s \nabla_{\boldsymbol{n}} V / R_{\square}$ can be calculated, where the integral runs along an arbitrary line cutting the source–drain path. It is convenient to normalize V by $IR_{\square}$, since $V / IR_{\square}$ directly reflects the *number of squares* between different points within the metallic structure, i.e. the length-to-width ratio of a strip which would acquire an equivalent voltage drop if biased by the same current. Figure 2 shows the result of the calculation for a layout typically used in our experiments. The inset of this figure displays the power density in the centre of the structure. The notch in the middle does indeed lead to the intended peak of the power density at this position (and of the current density that drives EM). However, a similar peak is found at the crossover from the funnel-shaped leads to the narrow wire as indicated by the four lightly coloured spots at the rectangular corners in the inset of figure 2. This is due to the well-known divergence of the electric field strength at corners [29]. In our numerics, this divergence is limited only by the finite cell size used in the finite-difference method as corners are infinitely sharp in the layout. In practice, e-beam lithography leads to a minimal radius at corners set by the finite resolution of the process and the granularity of the crystalline metallic layers. This radius sets the scale of the actual current-density enhancements. It can thus be expected that the current density reaches the same order of magnitude at each concave corner. The precise value depends, however, on the opening angles and can be tuned by proper design. Consequently, rectangular corners as the ones visible in figure 2 should be avoided in the strongly heated parts of the structure, unless a starting point for EM is intended. We are going to comment further on this issue in the next section.
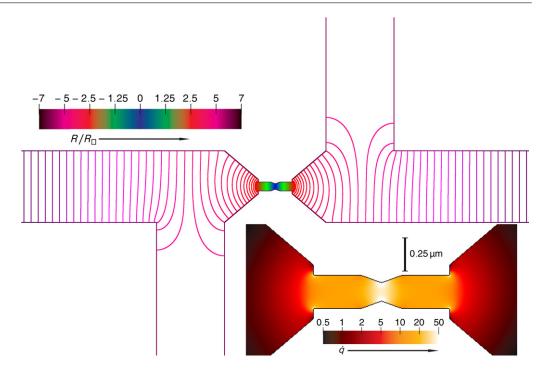
Figure 2. Equipotential lines for a test layout biased in horizontal direction. The taps pointing up- and downwards represent voltage probes. The voltage drop between consecutive lines is $\Delta V = 0.1 R_\square I$ and the total drop between the outermost lines $V = 12.4 R_\square I$. The inner region where the potential lines merge to a continuous colour scale corresponds to $\Delta V = 5 R_\square I$. The inset displays the resulting power density $\dot{q}$ in units of $I^2 R_\square \mu m^{-2}$ for the centre of the main figure. Notice the peaking of the power density at concave corners.

Having $\dot{q} = (\nabla V)^2 / R_\square$ at hand, we solve (1) and (2) simultaneously by an iterative procedure. Starting with $\delta T(r) = \delta T_s(r) = 0$ we first relax (1) at constant δT_s to get an updated estimate for $\delta T(r)$. The boundary conditions for the structure edges are again of von-Neumann type, $\nabla_n \delta T = 0$. Special care has to be taken to treat the heat flow at the border of the cutout. Owing to the aforementioned homogeneous nature of the leads extending beyond this border, the heat-flow problem is essentially one dimensional here [30]. In long leads the temperature elevation along the wire direction approaches exponentially a steady-state value of

$$\delta T_a = \delta T_s + I_\ell^2 R_\square b / (w^2 k_b),$$

where I_ℓ is the current in the specific lead of width w. In general, the substrate temperature δT_s in this equation has to be determined self-consistently as it results from the heat flow caused by the last term. However, δT_s is naturally small compared to more strongly heated zones below spots of high current density. We ignore small variations of δT_s at the border of the cutout and take in the above formula for δT_s a self-consistently calculated value. The functional dependence of the temperature along the leads is then given by

$$\delta T(x) = \delta T_a + (\delta T_0 - \delta T_a) \exp(-(x - x_0)/\lambda). \tag{4}$$

Here x is a spatial coordinate along the current direction leaving the cutout at x_0, δT_0 is the temperature elevation of the cross section at x_0 and $\lambda = \sqrt{bd k_m / k_b}$ is the length scale of

relaxation towards the asymptotic δT_a. From (4) the boundary condition of (1) at the cutout frame can be deduced,

$$\nabla_n \delta T = (\delta T_a - \delta T_0)/\lambda. \tag{5}$$

Equation (5) completes the boundary-value problem defined in (1) and is used in a successive overrelaxation loop to update $\delta T(\mathbf{r})$. In the next step of the iterative procedure we fix $\delta T(\mathbf{r})$ in (3) and update $\delta T_s(\mathbf{r})$ via (2). Here, successive overrelaxation would fail since the 3D nature of heat relaxation in the substrate leads to an intractably large number of cells in the discretization step. The final goal of our calculation, however, is the determination of $\delta T(\mathbf{r})$ defined in the two-dimensional plane of the metallic structure. To this end we need to know $\delta T_s(\mathbf{r})$ at the interface between the substrate and the barrier only. Let $G(\mathbf{r})$ be the solution of $\nabla^2 G = 0$ in the 3D half-space of $z < 0$ obeying Dirichlet conditions $G(\mathbf{r} \to \infty) = 0$ and von-Neumann conditions at $z = 0$, $\nabla_n G = \delta(\mathbf{r})$. Due to the linearity of the Laplace equation we can write down immediately the solution of (2) obeying the boundary condition of (3),

$$\delta T_s(\mathbf{r}) = \frac{k_b}{bk_s} \int d\mathbf{r}' G(\mathbf{r} - \mathbf{r}') \left(\delta T(\mathbf{r}') - \delta T_s(\mathbf{r}') \right). \tag{6}$$

The integral is restricted to the plane $z = 0$. Thus, the calculation of $\delta T_s(\mathbf{r})$ at the interface $z = 0$ requires the knowledge of $G(\mathbf{r})$ at the interface only as well. In this way (6) is reduced to a two-dimensional convolution which can be solved numerically by discrete Fourier transforms (DFT) for which fast algorithms exist. Our problem is thus reduced to the determination of $G(\mathbf{r})$. Details of this calculation are given in the appendix.

Equation (6) can now be used to update $\delta T_s(\mathbf{r})$. Note, however, that (6) does define δT_s only implicitly. Therefore a further relaxation loop is required. In each iteration of this loop the convolution on the right-hand side is calculated employing the convolution theorem by two consecutive DFT steps. The result is subsequently used to update δT_s. In the course of the iteration, the changes in δT_s get smaller and the loop is terminated after sufficient accuracy has been obtained. This ends the first round of our overall iterative procedure. In the following iterations we proceed by using (1) at constant δT_s to update δT and (2) at constant δT to update δT_s. The procedure converges to a self-consistent solution after several iterations.

So far we have developed a model applicable for thin barrier thickness b. From now on, we refer to this particular treatment as approximation I. In the next section we present results showing that indeed substrate temperature δT_s and δT follow each other closely for small b and the *a priori* approximation of a laminar heat flow perpendicular to the interface between substrate and barrier is justified in this case. However, δT_s is a monotonically decreasing function of b while at the same time δT rises monotonically. Moreover, at small b it is possible to heat the substrate rather locally by the large power density resulting from a notch as, e.g. the one in the centre of the test structure displayed in figure 2. If b is increased the power is delivered to the substrate more evenly and the temperature distribution tends to smooth out (with a small enhancement only even at the centre). The temperature difference $\delta T - \delta T_s$ soon becomes so large that δT_s on the right-hand side of (1) can safely be neglected. In this case, the vertical nature of the heat flow is lost and the problem of the heat distribution in the isolating barrier has to be treated more precisely. Fortunately, this can be done by the same method introduced so far. For thicker barriers we take the temperature at the interface of the substrate with the barrier as unelevated, the barrier now stays cold at its back side and takes thus the role formerly played

by the substrate. The set of equations (1)–(3) now reads

$$k_{\mathrm{m}} d \nabla^2 \delta T + \dot{q} = k_{\mathrm{b}} \frac{\Delta \delta T}{\varepsilon}, \quad \nabla^2 \delta T_{\mathrm{s}} = 0, \quad \nabla_{\boldsymbol{n}} \delta T_{\mathrm{s}} = -\frac{\Delta T}{\varepsilon}, \quad (7)$$

where ΔT is the temperature drop across a slice of the barrier of infinitesimal thickness ε. In the finite-difference treatment of the problem we set ε equal to the discretization cell size. In (7) $\delta T_{\mathrm{s}} = \delta T_{\mathrm{s}}(\boldsymbol{r})$ represents the 3D temperature profile in the *barrier*. As such, it is defined at the interface of the barrier with the metal film, too. At this interface, δT_{s} equals δT (in the numerics it differs marginally since the infinitesimal ε is approximated by a variable of finite extent). The thickness b enters this approximation via a modification of $G(\boldsymbol{r})$ in (6), which we label $G_b(\boldsymbol{r})$. It still obeys the Laplace equation $\nabla^2 G_b = 0$, now in the barrier, i.e. for $-b < z < 0$, but the Dirichlet condition $G(\boldsymbol{r} \to \infty) = 0$ is replaced at $z = -b$ by $G_b(z = -b) = 0$. In this way we approximate the temperature at the interface between barrier and substrate by the base temperature of the unbiased sample. We refer to this variant of the model as approximation II in the following section. The calculation of $G_b(\boldsymbol{r})$ on a rectangular grid used in the finite-difference approximation is explained in the appendix.

4. Results

The model developed in the last section can be used to optimize structure layouts intended for the formation of narrow break junctions at well defined locations by deliberate electromigration. In this section we present some examples.

First we want to address the question why metallic structures on a thicker silicon oxide layer are more likely to melt during the EM process than samples on native SiO$_2$. For that purpose we calculate the excess-temperature map for the sample geometry shown in figure 2 for varying barrier height b. For definiteness we consider gold structures ($k_{\mathrm{m}} \approx 316\,\mathrm{W\,K^{-1}\,m^{-1}}$ [31]) with a layer thickness of $d = 30\,\mathrm{nm}$, approximate the thermal conductivity of the substrate by the typical value of silicon at room temperature, $k_{\mathrm{s}} \approx 150\,\mathrm{W\,K^{-1}\,m^{-1}}$ [32], and vary b between 1 nm and 2.5 μm. For the thermal conductivity of the barrier we use that of thin SiO$_2$ films at room temperature, $k_{\mathrm{b}} \approx 1.1\,\mathrm{W\,K^{-1}\,m^{-1}}$ [33].

Figure 3 shows the results for $b = 1$, 100 and 1 μm. Obviously, the temperatures of substrate and metallic structure follow each other closely for very thin barriers (see figures 3(a) and (b)). For thicker barriers the asymptotic temperature δT_{a} in the leads can easily reach values that exceed the maximum temperature for thin barriers (compare figures 3(a) and (c), calculated with approximation I, i.e. a 3D heat relaxation in the substrate and a vertical laminar flow in the barrier). The temperature is maximal at the centre of the wire as expected. A typical value for the sheet resistance is $R_{\square} = 2\,\Omega$, so that $I^2 R_{\square} = 1\,\mathrm{mW}$ at around $I = 20\,\mathrm{mA}$. For this current a moderate temperature rise of $T_{\mathrm{max}} \approx 50\,\mathrm{K}$ results at the centre of the narrow wire, if the barrier thickness $b = 1\,\mathrm{nm}$. For $b = 100\,\mathrm{nm}$ the temperature rises already by $T_{\mathrm{max}} \approx 510\,\mathrm{K}$. The substrate temperature below the leads, however, does not change significantly for thicker barriers due to the fact that the substrate underneath long leads is heated by the power density $I^2 R_{\square}/w^2$ independent of barrier thickness (compare figures 3 (b) and (d)). For $R_{\square} = 2\,\Omega$ we get a marginal warming by about 1.6 K at $I = 20\,\mathrm{mA}$. Furthermore, substrate heating below the centre of the wire is reduced with increasing b. Between $b = 1$ and 100 nm the maximum temperature rise in the substrate drops from about 30 to 10 K. This is a rather low temperature increase as compared to the rise in the metallic structure, i.e. approximation II is a better
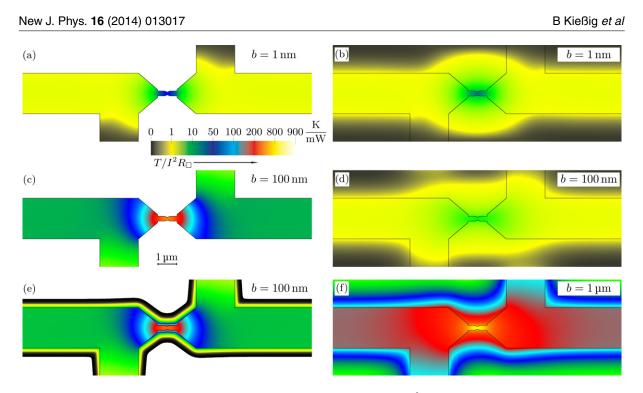
Figure 3. Maps of normalized temperature, $\delta T/I^2 R_\square$, of metallic structure ((a) and (c)), substrate–barrier interface ((b) and (d)), and interface between barrier and metallic structure ((e) and (f)). Colours are according to the scale in units of $K\,mW^{-1}$. Results for three barrier thicknesses are shown: $b = 1\,nm$ ((a) and (b)), $b = 100\,nm$ ((c)–(e)), and $b = 1\,\mu m$ (f). Panels (a)–(d) are calculated with approximation I, while for (e) and (f) approximation II is used.

choice for $b \gtrsim 100\,nm$. Figure 3(e) displays the temperature profile in the plain defined by the interface between the barrier and metal film calculated in the framework of approximation II, i.e. evaluating the 3D heat relaxation in the barrier, while the substrate is assumed to remain cold. Approximations I and II lead to similar results at $b = 100\,nm$ as can be judged by inspecting figures 3(c) and (e). Barrier heating is restricted mainly to the regions underneath the metallic structure for $b = 100\,nm$ with a small halo only. At larger b (see figure 3(f)), however, the area of the barrier with a significant temperature rise has a considerably larger extent. Nevertheless, a pronounced maximum of the temperature in the central spot of the structure remains the dominant feature[4].

Data for further values of b are summarized in figure 4, where the temperature profile along the central axis is displayed. The successive rise of the asymptotic lead temperature δT_a with b for $|x/L| \gtrsim 4$ is the most prominent feature in this figure. Furthermore, one can observe that the ratio between the maximum temperature in the centre and δT_a is strongly reduced with increasing b. For $b = 100\,nm$ results of approximation I and II are included. Both approximations yield similar results at this thickness, with slightly lower values of δT for

---

[4] Our model does not take into account the effect of radiation cooling because the latter is negligible. The radiation losses are bounded by $\sigma T_m^4 \approx 0.2\,\mu W\,\mu m^{-2}$ (σ is the Stefan–Boltzmann constant and $T_m = 1337.33\,K$ the melting point of gold) and thus several orders of magnitude smaller than the power carried by heat transport in case of significant heating.
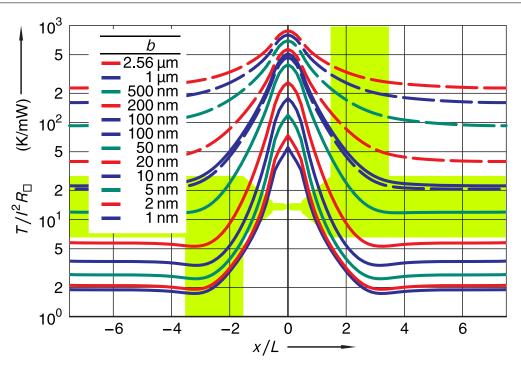
Figure 4. Excess temperature δT along the central axis of the same structure as used in figure 3. Note the logarithmic vertical scale. A picture of the structure has been underlayed to ease matching regions of different current densities with the shown curves. $L = 1\,\mu$m is defined as the length of the narrow wire in the centre. The thickness b of the SiO$_2$ barrier is varied between 1 nm and 2.56 μm, the temperature is normalized by $I^2 R_\square$. Solid lines correspond to approximation I, while dashed lines are calculated using approximation II.

approximation II due to the more efficient cooling resulting from the temperature halo around the metallic structure visible in figure 3(e).

In a well accepted approximation [1], the amount of gold pushed in the anode direction is proportional to both the current density and the self-diffusivity of the metal. The latter has a strong temperature dependence described over a wide range by an Arrhenius law [34] (for self-diffusion data on Au see e.g. [35–38]). Independent of the microscopic details of EM, however, a sizeable effect sufficient for the deliberate formation of voids requires elevated temperatures. As a rule of thumb, δT should be at least half the melting temperature $T_{\rm m}$, in which case EM along grain boundaries is in general the dominant material flux mechanism. The effect of EM is much stronger just below melting and is then in general dominated by flux within the bulk. However, for a controlled process of gap formation the melting point must not be exceeded. This is the crucial point discussed here. In figure 5(a) we plot $\alpha = \sqrt{1/y_{\rm max}}$ as a function of b, where $y_{\rm max}$ are the maximal values of the curves in figure 4 at $x = 0$, where the temperature in the metallic structure is highest. If we fix the temperature elevation at a value δT_0 well below the melting point (let us say at $\delta T_0 \approx 1000\,$K for gold, the exact choice of δT_0 is not important for our conclusion) $I_0 = \alpha \sqrt{\delta T_0/R_\square}$ directly gives a safe current limit for the specific structure. This safe current limit is considerably reduced when b is increased as shown in figure 5(a). For a native oxide barrier of $b \sim 1\,$nm and $R_\square \approx 2\,\Omega$ a current of almost 100 mA can be tolerated. For the thermally grown oxide layer of our experiments ($b = 400\,$nm) the safe current limit is by
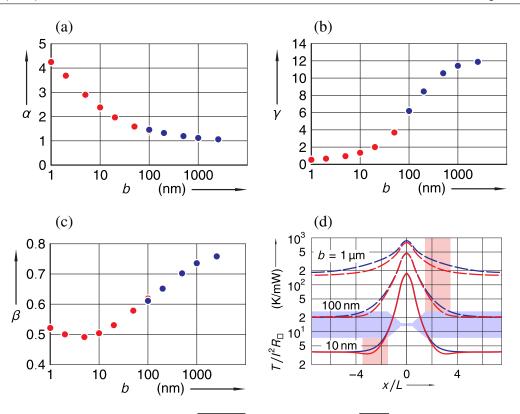
Figure 5. (a) Plot of $\alpha = I\sqrt{R_\square/\delta T_0}$ in units of $\text{mA}\sqrt{\Omega/\text{K}}$ as a function of the barrier thickness b. Here I is the current needed to heat the structure of figure 3 in its centre to a temperature δT_0. (b) Ratio γ of the first term in (1) to the negative of the term on the right hand side of the same equation in the centre of the structure, $\gamma = (dbk_\text{m}/k_\text{b})\nabla^2\delta T/(\delta T_\text{s} - \delta T)$. This compares the amount of heat flow in the metal to the effect of cooling by the substrate. At large b the structure is thermally decoupled in its centre. (c) Ratio $\beta = \delta T_1/T_\text{max}$ of the temperature δT_1 at the crossover from the narrow wire to the funnel-shaped parts of the leads and the temperature T_max in the centre as a function of b. Red dots in (a)–(c) are calculated with approximation I, blue dots with approximation II. (d) Temperature profile along the central axis of two different structures at $b = 10$, 100 and 1000 nm. The bluish and reddish underlay indicate current and voltage probes, respectively. Red lines correspond to results for the four-point configuration shown in figure 3 (complete underlay). Blue lines are calculated for a two point configuration, i.e. the voltage probes are missing (bluish underlay only). For $b = 10$ nm approximation I and for larger b approximation II has been used.

a factor of four smaller. This makes controlled EM considerably more difficult. The feedback loop as implemented by us and others [17] uses a resistance change to judge the appropriate current density. This procedure however might lead to current densities that exceed the limit set by the melting point of gold and thus to a failure of EIBJ formation.

It is instructive to compare the size of the first term in (1), i.e. the heat transport in the metallic structure, to the size of the right-hand side of the same equation, i.e. the heat flow to the substrate. This is done in figure 5(b) for the central point $x = 0$ of the structure where the temperature for a given current I is highest. The ratio

$$\gamma = (dbk_\text{m}/k_\text{b})(\nabla^2\delta T/(\delta T_\text{s} - \delta T))$$

of these two terms is considerably smaller than 1 for $b \lesssim 5$ nm, i.e. the centre of the structure is efficiently cooled via the substrate. For larger b, however, γ rises quickly indicating that the coupling to the substrate becomes increasingly inefficient and cooling has to rely on the heat flow along the metallic leads. The barrier thickness at which this decoupling sets in is expected to be reduced with decreasing width of the notch in the centre. Thus, if void formation by EM occurs and the current path through a narrowing constriction, temperature is dominated more and more by the heat flow along the structure. This leads to an even stronger tendency towards melting which has to be counteracted by increasingly careful settings in the feedback-control loop and necessitates good thermal coupling from the beginning. In summary, our analysis gives clear evidence why controlled electromigration on thick oxide barriers is more likely to fail.

Figure 5(c) displays the ratio β of the temperatures at the wire end (i.e. at the crossover from the narrow region to the funnel-shaped parts of the leads) and at the centre, as a function of b. Ideally, the temperature peaks so strongly at the centre that EM acts only there with reasonable strength. This is difficult to achieve, though. Figure 5(b) indicates that an optimal barrier thickness b_{opt} exists at which $\beta(b_{opt}) \approx 0.5$. This factor-of-two reduction of the temperature is not sufficient as demonstrated by the experimental result presented in figure 1(a). As indicated in the inset of figure 2 the current density peaks not only at the notch in the centre but at concave corners as well. EM leads to material flux in regions of high current density. The formation of voids or hillocks, in turn, requires some kind of inhomogeneity that causes a divergence of material flux. Such an inhomogeneity might be simply due to the statistical distribution of grains comprising the metallic structure, but regions of high temperature gradient lead for sure to a divergence in atomic flux as the delivery of material from cold regions is less efficient than delivery of material to the hotter parts. In the structure studied here the temperature gradient is large at the wire end and vanishes in the centre where the notch is located. In the latter position material transport tends to be balanced and thus the wire cross-section does not change to first order. Only at the corner at the cathode end void formation is favoured.

Figure 5(d) compares calculations for two different structures, namely the four-probe configuration with source and drain contacts and two voltage probes studied so far, and a two-probe configuration with no voltage probes. Clearly the temperature is reduced in the vicinity of the current-free voltage probes. However, their cooling effect is confined to a small region whose extent is set by the relaxation parameter $\lambda = \sqrt{bdk_m/k_b}$ in (4). The design of cooling fins would require to place them within a distance set by λ. For the model parameter used in our calculations $\lambda \sim 290$, 930 nm, and 2.9 μm for $b = 10$, 100 nm and 1 μm, respectively. The voltage probes in our test structure are within the range of the central notch for $b = 1 \mu$m, only. Consequently, the temperature is slightly reduced in the centre in this case as can be seen in figure 5(d). Note, however, that the temperature in the centre of the structure is peaking on top of the asymptotic temperature δT_a and this temperature scales quadratically with $1/w$, the width of the source and drain leads. Thus, a stronger reduction can be obtained by making the leads as wide as possible.

To demonstrate the application of our numerical simulations for the optimization of the sample layout with respect to control over the location where gap formation sets in, we design a structure in which the current path branches into a loop (see figure 6). The final goal with this specific structure is to produce two gaps, one in each loop arm. If bridged by molecules, such a sample could be used to test for the quantum coherence of electron transport through molecules by measuring the magnetoconductance. Coherence would lead to the appearance of periodic oscillation of the conductance in response to the magnetic flux penetrating the area
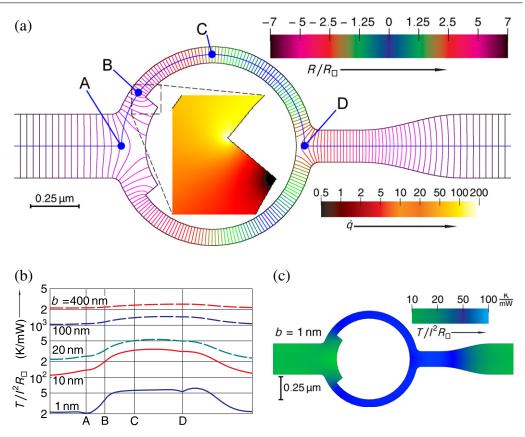
Figure 6. (a) Equipotential lines for a ring structure. The voltage drop between consecutive lines is $\Delta V = 0.1 R_\square I$ and the total voltage drop between the outermost lines is $\Delta V = 13.8 R_\square I$. The enlarged detail shown in the ring centre displays the power density in units of $I^2 R_\square \mu\text{m}^{-2}$ (see colour scale on the right bottom). (b) Temperature profile along the blue line in (a) for various barrier thicknesses. Solid lines are calculated with approximation I and dashed lines with approximation II. (c) Temperature map of the ring structure with a barrier thickness of $b = 1\,\text{nm}$ according to approximation I.

between the loop arms [39]. In the design of figure 6(a) we try to avoid unintentional current density enhancements by rounding all concave corners. A step in the width of the current path is introduced only at two positions. The inset in the ring centre of figure 6(a) demonstrates that this leads to a considerable current-density enhancement at singular points. At the same time we would like to have a large temperature gradient at this location. To this end we make the current path twice as narrow on the anode side of the ring structure and thus the power density by a factor of four larger. The investigation of coherent transport requires a high aspect ratio of the open area between the loop arms and the part of the ring area covered by metal. For this reason, the step in the ring width is placed close to the cathode side of the structure. Figure 6(c) shows the result of approximation I for a thin barrier ($b = 1\,\text{nm}$). The temperature changes abruptly at the transition from the wide to the narrow part of the ring thus making the concave corner at this position a preferred starting point for void formation. In figure 6(b) we display the temperature profile along the path drawn as a blue line in figure 6(a) for various barrier thicknesses. The temperature gradient is large at point B for a thin barrier as intended. The temperature reaches to first approximation almost constant values to the left of point A and between point C and D for $b = 1\,\text{nm}$ on account of a short relaxation parameter

$\lambda \sim 290$ nm. With increasing thickness b, however, Joule heating leads to a more evenly distributed temperature due to the rise in $\lambda \propto \sqrt{b}$. As a result, the temperature gradient at point B gets more and more shallow making the tendency to void formation at the corner weaker. Still, EM is boosted by the current-density rise at this location which is thus distinguished from the rest of the structure. Nevertheless, the statistical nature of grain boundaries easily marks different locations along the line from B to D where void formation might start. Hence, it is not clear from the outset that the corner close to point B will win for larger b. This again stresses that reliable void formation is favoured by good thermal coupling via a thin barrier to a substrate of high thermal conductance.

5. Limitations of the model

The electro-thermal model presented here can be used to calculate the current density and temperature profile for planar structures. The solution of this model can give hints on where EM most likely leads to vacancy accumulation and void nucleation. Once void nucleation has taken place the void is likely to grow and a break junction will form in close proximity to the initial nucleation centre. A more complete calculation might try to simulate the actual EM process including the problem of the vacancy dynamics, void nucleation and evolution and thus would model the time evolution of EIBJ formation [4]. This, however, is a much more ambitious task and not the purpose of the present work. In our opinion it would blur the statements we make. As already noted, the exact position of void nucleation in an actual sample will depend on details of the microscopic arrangement of disorder and large sample-to-sample fluctuations will be observed. Grain boundaries play a major role in the process and the position of grain boundaries is hard to control in sample fabrication. However, it is not the fluctuations between samples we want to model but rather the averaged position of the final break junction. For this purpose our calculation on a homogenized representation of an ensemble of samples is an appropriate starting point.

In the present paper we also avoided to include temperature dependent electrical and thermal conductivities which would have made the calculation much more cumbersome. The inclusion of temperature dependent parameters would first of all require a reliable model of this dependence. For the thermal conductivity of Si and SiO_2 this is a simple task. In most cases the silicon substrate is only modestly heated and the change in thermal conductivity thus marginal. The temperature dependence of the thermal conductivity of SiO_2, on the other hand, is much weaker and is hardly increased by more than 50% even under extreme conditions. Thus the most pronounced effect can be expected to result from the temperature dependences of $R_\square$ and k_m of the metallic structure. Here a reliable model is not at hand.

Before EM leads to depletion of material a pronounced lowering of the overall resistance is observed: R/V characteristics are shifted to smaller R values (see video clips in the supplementary material (available from stacks.iop.org/NJP/16/013017/mmedia)) due to the annealing of defects and decreasing disorder as a result of heating. The temperature dependence of the resistance is not very strong. At a sheet resistance of $2\,\Omega$ the Drude mean free path is of the order of $\ell = 14$ nm. This value does nicely correspond to the granularity of the metallic film, as can be judged by inspection of SE micrographs. The bulk value of the mean free path of gold at room temperature, on the other hand, is $\ell = 34$ nm and is connected largely to phonon scattering. Thus the resistance of our thin film structures is dominated by disorder scattering of conduction electrons as typical for nanoscaled metallic samples. By heating up we have a

decrease of disorder and phonon scattering takes over. For example, at 900 K phonon scattering alone results in $\ell = 10$ nm. At this temperature we expect pronounced material flow caused by EM. As a result we observe experimentally signs of crystal growth; grains are merged into growing single-crystalline regions which show in many cases facets (see the video clip supplied as supplementary material). In view of resistance, we have a reduction of disorder scattering counteracted by a stronger scattering by phonons. Thus, while it might be difficult to model the resistance as a function of Joule heating, it has supposably a noticeable but small effect. This is supported by the success of our simple model. Similar arguments apply to thermal conductance.

Still, it might by tempting to explore models including temperature and position dependent parameters. Such a model is currently under construction. It will include a temperature dependent sheet resistance $R_\square(\boldsymbol{r}, T)$ and use a thermal conductivity assuming the validity of the Widemann–Franz law. Preliminary results indicate that the main conclusion of our paper is not substantially altered although the overall temperature profile is slightly different for a large current in the improved model. In particular, the $\delta T(x/L)$ profile (see figures 4 and 5(d)) will sharpen somewhat for small x/L. Consequentially the safe-current limit as defined in the discussion of figure 5(a) will be reduced. Thus, it will be even more difficult not to exceed the safe-current limit in the case of EM performed on samples with thick barriers. Hence the main conclusion of our experiments, i.e. that thin barriers are mandatory for EIBJ fabrication in planar structures, is theoretically corroborated by this qualitative argument.

6. Conclusion

In this paper we have presented experimental results showing that nanogap formation by EM depends crucially on the thickness of an insulating barrier between a planar metallic structure and a thermally well conducting substrate. We have developed a numerical model which explains these findings by considering the strength of thermal coupling of the metallic structure to the substrate. Only for thin barriers is cooling by heat flow to the substrate efficient, while for thick barriers the temperature is governed only by heat flow along the leads connecting the microstructures to regions of lower current densities. Thus, only thin barriers allow the large current densities required for void formation on a reasonable time scale without melting large parts of the structure by Joule heating. Therefore, good thermal coupling is an important prerequisite for well controlled EM. On the other hand, thin barriers are not always an option in practice. The native oxides on silicon wafers have been reported to be as thin as 1 nm. While such a thin barrier yields a good thermal contact it bears the risk of undesirable electrical leakage currents through the substrate. For a reliable electrical insulation of the structure a barrier of several 100 nm thickness is mandatory.

In our model calculation we considered cooling the structure by coupling it to a cold substrate. In practice, heat can be released by other means. If EM has to be performed in vacuum for some reason, the only possibility might be to fabricate leads and microstructure from metallic layers of different thickness [14, 15, 19, 22, 40–42]. If the leads are thicker than the microstructure, the positive influence on EIBJ control is two fold. Firstly, the heat conductance is increased and secondly, the self heating of the leads is reduced due to the lower current density; the lead thus stay colder than their counterpart in planar structures and the temperature of the microstructure itself is reduced accordingly. Unfortunately, the implementation of thick leads or more general leads with large cross section limits the geometric freedom of possible layouts.

A good example where leads of large cross section cannot be tolerated is the ring structure presented in the last section. Here larger leads would automatically reduce the visibility of the Aharonov–Bohm oscillations which are the purpose of the experiment in the first place. If it is possible to execute EM in a controlled atmosphere, the gas can be utilized for cooling. We have, e.g. performed EM experiments in the gas phase above the liquid level of a helium dewar. The structure heated by a high current density leads to convection of the cold gas which in turn gives rise to an efficient heat release. The yield of sufficiently small nanogaps is considerably increased in this case even on thick SiO_2 barriers. Whether the resulting gaps are clean and not contaminated with metallic nano-clusters is an open question at this moment [11–13].

Besides efficient heat release, a good layout design is needed to predefine the position of void formation. The latter starts preferably at positions where high current densities meet large temperature gradients. It is thus advisable not to place the intended gap position in high symmetry points of the layout where temperature gradients are expected to vanish but to mark it with sharp corners which can be utilized for a considerable current density enhancement.

Acknowledgments

Appendix. Calculation of $G_b(r)$

$G_b(\boldsymbol{r})$ resembles closely the Green's function $G_b(\boldsymbol{r}) = G(\boldsymbol{r}, 0)$ of the Laplace operator defined by $\nabla^2 G(\boldsymbol{r}, \boldsymbol{r}') = \delta(\boldsymbol{r} - \boldsymbol{r}')$. The integral in (6) runs over the plane $z = 0$. So, the second argument in $G(\boldsymbol{r}, \boldsymbol{r}')$ is restricted to this plane. Due to invariance of the problem with respect to shifts by $\delta \boldsymbol{r} = (x, y, 0)$, $G(\boldsymbol{r}, \boldsymbol{r}')$ does depend on the difference of its arguments only. $G_b(\boldsymbol{r})$ obeys the source free Laplace equation for $z < 0$ with a flux of unit strength flowing into the surface at $\boldsymbol{r} = 0$. At the opposite boundary, $z = -N_z h$, G_b vanishes (Dirichlet condition).

We calculate $G_b(\boldsymbol{r})$ by discrete cosine transform (DCT) on a cube of $N \times N \times N_z$ cells ($N = 1024$ turns out to be sufficient) with the basic approach

$$G_b(x, y, z) = \sum_{X,Y=0}^{n-1} \sum_{Z=0}^{N_z-1} \widehat{G}_b(X, Y, Z) \cos(\pi x(X + 1/2)/n) \cos(\pi y(Y + 1/2)/n)$$
$$\times \cos(\pi(z + 1/2)(Z + 1/2)/N_z), \tag{A.1}$$

where $n = N/2$ and the arguments of the cosine functions are chosen to assure $G_b(\pm n, y, z) = G_b(x, \pm n, z) = G_b(x, y, N_z - 1/2) = 0$, $\quad G_b(1, y, z) = G_b(-1, y, z)$, $\quad G_b(x, 1, z) = G_b(x, -1, z)$ and $G_b(x, y, 0) = G_b(x, y, -1)$. Together with the discrete version of the Poisson equation

$$D^2 G = \delta_{xyz}, \tag{A.2}$$

this describes a single source of unit strength at $(x = 0, y = 0, z = -1/2)$. D^2 is the discrete version of the Laplace operator ∇^2, $\delta_{000} = 1$ and $\delta_{xyz} = 0$ for all other combinations of the indices. From (A.2) one gets

$$\widehat{G}_b(X, Y, Z) = \widehat{q}(X, Y, Z)[4(\cos(\pi(X + 1/2)/n) + \cos(\pi(Y + 1/2)/n)$$
$$+ \cos(\pi(2Z + 1)/N_z)) - 3]^{-1}, \tag{A.3}$$

where $\widehat{q}(X, Y, Z)$ is the DCT of δ_{xyz} defined with the same arguments in the cosine functions as in (A.1). Thus the calculation of $G_b(\boldsymbol{r})$ involves two DCT operations and normalization of the intermediate result according to (A.3). The index b enters into the calculation via the definition of $N_z = b/h$, where h is the discretization size in the finite-difference method. For approximation I we need to know $G(\boldsymbol{r}) = \lim_{b \to \infty} G_b(\boldsymbol{r})$. We approximate it by setting $G(\boldsymbol{r}) \approx G_{512}$, which is sufficiently accurate due to the asymptotic $1/r$ nature of the analytical solution.

References

[1] Ho P S and Kwok T 1989 Electromigration in metals *Rep. Prog. Phys.* **52** 301–48

[2] Sorbello R S 1998 Theory of electromigration *Solid State Physics, Advances in Research and Application* vol 51 ed H Ehrenreich and F Spaepen (San Diego, CA: Academic) pp 159–231

[3] Sorbello R S 1972 A pseudopotential based theory of the driving forces for electromigration in metals *J. Phys. Chem. Solids* **34** 937–50

[4] de Orio R L, Ceric H and Selberherr S 2010 Physically based models of electromigration: from black's equation to modern TCAD models *Microelectron. Reliab.* **50** 775–89 and references therein

[5] Demarchi D, Civera P, Piccinini G, Cocuzza M and Perrone D 2009 Electrothermal modelling for EIBJ nanogap fabrication *Electrochim. Acta* **54** 6003–9

[6] Blech I A 1976 Electromigration in thin aluminum films on titanium nitride *J. Appl. Phys.* **47** 1203–8

[7] Park H, Lim A K L, Alivisatos A P, Park J and McEuen P L 1999 Fabrication of metallic electrodes with nanometer separation by electromigration *Appl. Phys. Lett.* **75** 301–3

[8] Blech I A and Kinsborn E 1975 Electromigration in thin gold films on molybdenum surfaces *Thin Solid Films* **25** 327–34

[9] Suo Z 2003 Interfacial and nanoscale fracture *Comprehensive Structural Integrity* vol 8 ed I Milne, R O Ritchie and B Karihaloo (Amsterdam: Elsevier) chapter 8.08 pp 265–324

[10] Park H, Park J, Lim A K L, Anderson E H, Alivisatos A P and McEuen P L 2000 Nanomechanical oscillations in a single-C-60 transistor *Nature* **407** 57–60

[11] Houck A A, Labaziewicz J, Chan E K, Folk J A and Chuang I L 2005 Kondo effect in electromigrated gold break junctions *Nano Lett.* **5** 1685–8

[12] Heersche H B, de Groot Z, Folk J A, Kouwenhoven L P, van der Zant H S J, Houck A A, Labaziewicz J and Chuang I L 2006 Kondo effect in the presence of magnetic impurities *Phys. Rev. Lett.* **96** 017205

[13] van der Zant H S J *et al* 2006 Molecular three-terminal devices: fabrication and measurements *Faraday Discuss.* **131** 347–56

[14] Strachan D R, Smith D E, Johnston D E, Park T-H, Therien M J, Bonnell D A and Johnston A T 2005 Controlled fabrication of nanogaps in ambient environment for molecular electronics *Appl. Phys. Lett.* **86** 043109

[15] Esen G and Fuhrer M S 2005 Temperature control of electromigration to form gold nanogap junctions *Appl. Phys. Lett.* **87** 263101

[16] Strachan D R, Smith D E, Fischbein M D, Johnston D E, Guiton B S, Drndić M, Bonnell D A and Johnston A T 2006 Clean electromigrated nanogaps imaged by transmission electron microscopy *Nano Lett.* **6** 441–4

[17] Hoffmann R, Weissenberger D, Hawecker J and Stöffler D 2008 Conductance of gold nanojunctions thinned by electromigration *Appl. Phys. Lett.* **93** 043118

[18] Wu Z M, Steinacher M, Huber R, Calame M, van der Molen S J and Schönenberger C 2007 Feedback controlled electromigration in four-terminal nanojunctions *Appl. Phys. Lett.* **91** 053118

[19] Taychatanapat T, Bolotin K I, Kuemmeth F and Ralph D C 2007 Imaging electromigration during the formation of break junctions *Nano Lett.* **7** 652–6

[20] Durkan C, Schneider M A and Welland M E 1999 Analysis of failure mechanisms in electrically stressed Au nanowires *J. Appl. Phys.* **86** 1280–6

[21] Lambert M F, Goffman M F, Bourgoin J P and Hesto P 2003 Fabrication and characterization of sub-3 nm gaps for single-cluster and single-molecule experiments *Nanotechnology* **14** 772–7

[22] Trouwborst M L, van der Molen S J and van Wees B J 2006 The role of Joule heating in the formation of nanogaps by electromigration *J. Appl. Phys.* **99** 114316

[23] Rattalino I, Motto P, Piccinini G and Demarchi D 2012 A new validation method for modeling nanogap fabrication by electromigration, based on the resistance–voltage $(R − V)$ curve analysis *Phys. Lett.* A **376** 2134–40

[24] Blech I A and Meieran E S 1967 Direct transmission electron microscope observation of electrotransport in aluminum thin films *Appl. Phys. Lett.* **11** 263–6

[25] Blech I A and Meieran E S 1969 Electromigration in thin Al films *J. Appl. Phys.* **40** 485–91

[26] Blech I A and Meieran E S 1972 Erratum: electromigration in thin Al films *J. Appl. Phys.* **43** 762

[27] Heersche H B, Lientschnig G, O'Neill K, van der Zant H S J and Zandbergen H W 2007 *In situ* imaging of electromigration-induced nanogap formation by transmission electron microscopy *Appl. Phys. Lett.* **91** 072107

[28] Press W H, Teukolsky S A, Vetterling William T and Flannery B P 2007 *Numerical Recipies* (Cambridge: Cambridge University Press)

[29] Jackson J D 1999 *Classical Electrodynamics* (New York: Wiley)

[30] Durkan C 2007 *Current at the Nanoscale, An Introduction to Nanoelectronics* (London: Imperial College Press)

[31] Powell R W, Ho C Y and Liley P E 1966 Thermal conductivity of selected materials *Technical Report* NSRDS-NBS 8, National Bureau of Standards (www.nist.gov/data/nsrds/NSRDS-NBS-8.pdf)

[32] Glassbrenner C J and Slack G A 1964 Thermal conductivity of silicon and germanium from 3°K to the melting point *Phys. Rev.* **134** A1058–69

[33] Kleiner M B, Kühn S A and Weber W 1996 Thermal conductivity measurements of thin silicon dioxide films in integrated circuits *IEEE Trans. Electron Devices* **43** 1602–9

[34] Bakker H *et al* 1990 *Diffusion in Solid Metals and Alloys* (*Landolt–Börnstein, New Series, Group III* vol 26) ed H Mehrer (Berlin: Springer)

[35] Gupta D 1973 Grain-boundary self-diffusion in Au by Ar sputtering technique *J. Appl. Phys.* **44** 4455–8

[36] Gupta D 1973 Self-diffusion along dislocations in single-crystal Au films *Phys. Rev.* B **7** 586–94

[37] Gupta D and Asai K W 1974 Grain boundary self-diffusion in evaporated Au films at low temperatures *Thin Solid Films* **22** 121–30

[38] McLean M and Hirth J P 1968 Surface self-diffusion on gold *Surf. Sci.* **12** 177–88

[39] Webb R A, Washburn S, Umbach C P and Laibowitz R B 1985 Observation of h/e Aharonov–Bohm oscillations in normal-metal rings *Phys. Rev. Lett.* **54** 2696

[40] Campbell J M and Knobel R G 2013 Feddback-controlled electromigration for the fabrication of point contacts *Appl. Phys. Lett.* **102** 023105

[41] Johnston D E, Strachan D R and Charlie Johnson A T 2007 Parallel fabrication of nanogap electrodes *Nano Lett.* **7** 2774–7

[42] Umeno A and Hirakawa K 2009 Nonthermal origin of electromigration at gold nanojunctions in the ballistic regime *Appl. Phys. Lett.* **94** 162103